

Polystyrene/Polyolefin Elastomer Blends Loaded with Halloysite Nanotubes: Morphological, Mechanical, and Gas Barrier Properties

Mohammad Iman Tayouri, Sara Estaji, Seyed Rasoul Mousavi, Amirhosein Yazdanbakhsh, Sasan Nouranian, Holger Ruckdäschel,* and Hossein Ali Khonakdar*

Herein, a simple melt-blending method is utilized to disperse of halloysite nanotubes (HNTs) in polystyrene/polyolefin elastomer (PS/POE) blends. Based on morphological studies, the PS/POE/HNT nanocomposite containing up to 3 phr HNTs shows excellent nanofiller dispersion, while those filled with 5 phr HNTs exhibit nanofiller aggregation. To overcome the nanofiller aggregation issue, the polypropylene-grafted-maleic anhydride (PP-g-MA) compatibilizer is added to the PS/POE/HNT nanocomposite, which results in improved mechanical properties for the nanocomposite sheets. Furthermore, the addition of compatibilized HNTs to the PS/POE blends leads to decreased O₂ and N₂ gas permeabilities. Besides, incorporating POE, HNTs, and PP-g-MA leads to a decrease in water vapor transmission of PS. In the end, the experimentally-determined mechanical properties and gas permeabilities of the nanocomposite sheets are compared to those predicted by prevalent theoretical models, revealing a good agreement between the experimental and theoretical results. Molecular-dynamics simulations are also carried out to calculate the gas diffusion coefficients in the different sheets to further support the experimental findings in this study. Overall, the PS/POE/HNT/PP-g-MA nanocomposite sheets fabricated in this work demonstrate excellent mechanical and gas barrier properties; and hence, can be used as candidate packaging materials. However, the strength of the resulting PS/POE blend may be inferior to that of the virgin PS.

1. Introduction

Polymeric materials have attracted substantial interest in the packaging industry due to their low cost, ease of processing, high stability, light weight, and outstanding flexibility.^[1–4] Among the synthetic, non-polar polymers, polystyrene (PS) is widely used in the packaging industry thanks to its inexpensiveness, transparency, and rigidity.^[5–7] However, PS has downsides, including low ductility, high gas permeability, and non-biodegradability.^[8,9] Recent research has indicated that blending PS with other polymers and/or nanofillers can alleviate its inherent deficiencies.^[10,11] Polyolefin elastomer (POE), a synthetic polymer consisting of ethylene–butane rubber (EBR) or ethylene–octene copolymer (EOC) with high elongation at break but low tensile strength and Young's modulus,^[12,13] may be blended with PS to yield PS/POE sheets, which are desirable for packaging applications. For example, Kiani et al.^[14] incorporated 20 wt% POE into PS and demonstrated an improvement in the elongation


M. I. Tayouri, S. Estaji, S. R. Mousavi, A. Yazdanbakhsh, H. A. Khonakdar
Department of Polymer Processing
Iran Polymer and Petrochemical Institute
Tehran 1497713115, Iran
E-mail: h.khonakdar@ippi.ac.ir

S. Estaji
School of Chemical Engineering, College of Engineering
University of Tehran
Tehran 141556619, Iran

S. Nouranian
Department of Chemical Engineering
University of Mississippi
University City, MS 38677, USA

S. Nouranian
Center for Graphene Research and Innovation
University of Mississippi
University City, MS 38677, USA

H. Ruckdäschel, H. A. Khonakdar
Department of Polymer Engineering
University of Bayreuth
95447 Bayreuth, Germany
E-mail: Holger.Ruckdaeschel@uni-bayreuth.de

 The ORCID identification number(s) for the author(s) of this article can be found under <https://doi.org/10.1002/mame.202300080>

© 2023 The Authors. Macromolecular Materials and Engineering published by Wiley-VCH GmbH. This is an open access article under the terms of the Creative Commons Attribution License, which permits use, distribution and reproduction in any medium, provided the original work is properly cited.

DOI: 10.1002/mame.202300080

at break of the neat PS sheet by 860%. However, based on their observations, the tensile strength and modulus of the PS sheet were reduced by 4.2 and 142 MPa, respectively. Nemati et al.^[15] used reactive blending in a co-rotating twin-screw extruder to process PS, POE, and nanoclay, resulting in microphase-separated blend nanocomposite films. Their results revealed that incorporating nanoclay in the blend led to a reduction in CO₂ and N₂ permeability. The molecular dynamic simulation outcomes also confirmed the experimental trends seen in their work.

In general, the addition of mineral nanofillers to polymer blends may result in improved gas permeability, mechanical properties, and biocompatibility of the resulting nanocomposite sheets.^[16,17] One of the eco-friendliest and most cost-effective, abundant, and biocompatible inorganic nanofillers are halloysite nanotubes (HNTs). These high-modulus nanofillers (Young's modulus: ≈ 140 GPa) have a hollow, tubular, and spherical structure in which siloxane (Si–O–Si) and Al–OH groups are located on the outer tube surfaces and inner walls, respectively.^[18] The hydroxyl groups on the HNT surfaces are known to be responsible for the poor dispersion of HNTs in non-polar polymers when processed by melt blending.^[19] To deal with the nanofiller dispersion issue, a compatibilizer can be added to the polymer/HNT blend.^[20,21] The impact of nanoparticles on the mechanical properties and gas permeability of polymer blends has been extensively studied in packaging applications. For example, Kubade et al.^[22] observed that by adding surface-modified HNTs to polypropylene (PP)/acrylonitrile butadiene styrene blends, significant improvements in the tensile strength (by ≈ 5 MPa) and tensile modulus (by ≈ 160 MPa) of the polymer blend sheet were achieved. These improvements were attributed to the refinement in the nanocomposite sheet morphology as a consequence of the surface modification of the HNTs. In another work, Lee et al.^[23] studied the effect of nanosilica (SiO₂) on the mechanical properties of PP/POE blends in the presence of a compatibilizer. Their results revealed that incorporating 5 wt% SiO₂ in the blend increased the tensile strength and modulus of the polymer blend sheet by ≈ 3 and 39 MPa, respectively, while the elongation at break decreased by 25%. In a computational work by Ebadi-Dehaghani et al.,^[24] the authors reported on the reduction of O₂ gas permeability in compatibilized PP/PLA/nanoclay nanocomposite sheets by 93%. In another work, Abdullah et al.^[25] reported that the presence of HNTs improved the O₂ gas barrier properties of a polyvinyl alcohol/starch/glycerol/HNT nanocomposite sheet. By incorporating the HNTs, the amount of oxygen that could pass through the sheet decreased by 74.84%.

In our previous work,^[15] the effects of nanoclay on the morphology, crystallization, and gas permeability characteristics of immiscible PS/POE blends in the presence and absence of maleic anhydride (MAH) grafted PP (PP-g-MAH) as compatibilizer were investigated. In addition, molecular dynamics (MD) simulation was used to calculate the gas diffusion coefficients. In the present study, the effects of HNTs and PP-g-MAH on the mechanical and gas permeability of the PS/POE blends are investigated using both experimental and theoretical approaches. Furthermore, MD simulation is used to yield a deeper understanding of the gas transport in the PS/POE/HNT sheets.

2. Theoretical Models

2.1. Mechanical Properties

The following models can be applied to predict the mechanical properties of polymer blends, such as tensile modulus and tensile strength, in the presence and absence of nanofillers:

2.1.1. Parallel or Voigt Model

The Parallel or Voigt model estimates an upper bound for the tensile modulus of a two-component system based on the mixture law and isostrain condition.^[26]

$$E_{II} = E_m \varphi_m + E_d \varphi_d \quad (1)$$

where E_{II} , E_m , and E_d express the tensile modulus of the blend (or nanocomposite), matrix, and dispersed phase, respectively. Furthermore, φ_m and φ_d represent the matrix and dispersed phase volume fractions, respectively.

2.1.2. Series or Reuss Model

In contrast to the parallel model, the series or Reuss model can predict the lower bound of the tensile modulus of a blend (or nanocomposite) using the following equation^[27]:

$$E_{II} = \left[\left(\frac{\varphi_m}{E_m} \right) + \left(\frac{\varphi_d}{E_d} \right) \right]^{-1} \quad (2)$$

2.1.3. Hirsch Model

The combination of the two above-mentioned models results in the following equation:^[28]

$$E_{II} = x (E_m \varphi_m + E_d \varphi_d) + (1 - x) \left[\left(\frac{\varphi_m}{E_m} \right) + \left(\frac{\varphi_d}{E_d} \right) \right]^{-1} \quad (3)$$

where x and $1 - x$ are related to the upper and lower bounds of the modulus, and the parameter x can be measured using the curve fitting of the Hirsch model to experimental data.

2.1.4. Coran and Patel Model

This model contains the upper and lower bound moduli (E_1 and E_2 , respectively), as shown in Equation (4). The fit parameter (n) refers to the continuity and phase inversion of the polymer blends. This parameter includes dispersed particle form, inter-domain interference, molecular inter-penetrability, wetting, and thermodynamic compatibility.^[29]

$$E_{II} = x (E_1 - E_2) + E_2 \quad (4)$$

$$x = \varphi_H^n (n\varphi_S + 1) \quad (5)$$

where φ_H and $\varphi_S = 1 - \varphi_H$ denote the volume fractions of the hard and soft components, respectively.

2.1.5. Barentsen Model

The Barentsen model was proposed for materials with a 3D geometry and can be used for two different arrangements of phases as follows:^[30]

Parallel Model of Serial Linked Parts: For co-continuous morphology:

$$E_{II} = \frac{a^2 b E_1^2 + (a^3 + 2ab + b^3) E_1 E_2 + ab^2 E_2^2}{a E_2 + b E_1} \quad (6)$$

For matrix-dispersed morphology:

$$E_{II} = (1 - \lambda^2) E_m + \left[\frac{\lambda^2 E_m E_d}{\lambda E_m + (1 - \lambda) E_d} \right] \quad (7)$$

Series Model of Parallel Parts: For co-continuous morphology:

$$E_{II} = E_m \frac{\lambda^2 E_d + (1 - \lambda^2) E_m}{(1 - \lambda) \lambda^2 E_d + (1 - \lambda^2 + \lambda^3) E_m} \quad (8)$$

For matrix-dispersed morphology:

$$E_{II} = \frac{(a^4 + 2a^3 b) E_1^2 + 2(a^3 b + 3a^2 b^2 + ab^3) E_1 E_2 + (2ab^3 + b^4) E_2^2}{(a^3 + a^2 b + 2ab^2) E_1 + (2a^2 b + ab^2 + b^3) E_2} \quad (9)$$

In Equations (6)–(9), $\lambda^3 = \phi_d = 1 - \phi_m$, where a denotes the volume fraction of first component, $3a^2 - 2a^3 = \phi_m$, and $b = 1 - a$.

2.1.6. Guth Model

This model was developed to be used for fiber-like fillers such as HNTs. Therefore, it can be employed to blend nanocomposites, considering the HNT aspect ratio:^[31]

$$\frac{E_{II}}{E_m} = 1 + 0.67\alpha\varphi_f + 1.62(\alpha\varphi_f)^2 \quad (10)$$

where $\alpha = l/t$ denotes the aspect ratio of the fiber, l is the length of the fiber, and t corresponds to the thickness of the fiber.

2.1.7. Halpin–Tsai Model

This model was developed by Herman and Hill^[32,33] to predict the modulus of unidirectional nanocomposite sheets:

$$\frac{E_{II}}{E_m} = \frac{1 + 2\alpha\eta\varphi_f}{1 - \eta\varphi_f} \quad (11)$$

where $\eta = (E_f/E_m - 1)/(E_f/E_m + 2\alpha)$ denotes the shape parameter and is dependent on the loading direction and the filler geometry.

2.1.8. Hui–Shia Model

This model presupposes perfect interfacial bonding between the matrix and reinforcements:^[34]

$$\frac{E_{II}}{E_m} = \left[1 - \frac{\varphi_f}{4} \left(\frac{1}{\zeta} + \frac{3}{\zeta + \Lambda} \right) \right]^{-1} \quad (12)$$

$$\zeta = \varphi_f + \frac{E_m}{E_f - f E_m} + 3(1 - \varphi_f) \frac{(1 - g) \alpha^{-2} - \frac{g}{2}}{\alpha^{-2} - 1} \quad (13)$$

$$\Lambda = (1 - \varphi_f) \left(\frac{3(\alpha^{-2} + 0.25)g - 2(\alpha^{-2})}{\alpha^{-2} - 1} \right) \quad (14)$$

where $g = \alpha^{-1}\pi/2$.

2.1.9. Paul Model

This model is governed by the macroscopically homogenous stress in the components of the nanocomposites:^[35]

$$\frac{E_{II}}{E_m} = \frac{1 + \left(\frac{E_f}{E_m} - 1 \right) \varphi_f^{2/3}}{1 + \left(\frac{E_f}{E_m} - 1 \right) \left(\varphi_f^{2/3} - \varphi_f \right)} \quad (15)$$

where E_f is tensile modulus of the nanofiller.

2.1.10. Maxwell Model

The Maxwell model^[36] was introduced for nanocomposites containing well-dispersed fillers. This model can be expressed as follows:

$$\frac{E_{II}}{E_m} = \frac{1 + 2\varphi_f \left(\frac{E_f}{E_m} - 1 \right) / \left(\frac{E_f}{E_m} + 2 \right)}{1 - \varphi_f \left(\frac{E_f}{E_m} - 1 \right) / \left(\frac{E_f}{E_m} + 2 \right)} \quad (16)$$

2.1.11. Nielsen Model

In the following equation, Nielsen modified the Halpin–Tsai theoretical model:

$$\frac{E_{II}}{E_m} = \frac{1 + \chi\eta\varphi_f}{1 - \eta\psi\varphi_f} \quad (17)$$

where $\chi = 2.5(\alpha)^{0.645} - 1$ under the non-slippage condition.^[37] The parameter ψ relates to the maximum packing volume fraction (φ_M) of filler according to the following equation:

$$\psi = 1 + \left(\frac{1 - \varphi_M}{\varphi_M^2} \right) \varphi_f \quad (18)$$

2.1.12. Pukanszky Model

This model was developed to estimate the tensile strength of nanocomposites as follows:

$$\sigma_{yc} = \sigma_{ym} \frac{1 - \varphi_f}{1 + 0.25\varphi_f} \exp(\beta\varphi_f) \quad (19)$$

where σ_{yc} and σ_{ym} are the yield strengths of the nanocomposite and matrix, respectively, and β is an empirical parameter expressing the matrix–filler interaction degree in terms of the efficiency of load transfer between the matrix and filler.^[34]

2.1.13. Nicolais and Narkis Model

Nicolais and Narkis proposed the following equation to predict the tensile strength of nanocomposites, considering a cubic matrix reinforced with well-dispersed spherical particles:^[38]

$$\sigma_{yc} = \sigma_{ym} \left(1 - 1.21\varphi_f^{\frac{2}{3}} \right) \quad (20)$$

2.2. Gas Permeability

The Nielsen and Cussler models^[25,39] are two of the most widely used models for predicting the gas permeability of polymers reinforced with tube-like nanofillers. The Nielsen model can be expressed for regular and random dispersions of the nanofillers in Equations (21) and (22), respectively:

$$\frac{P_c}{P_o} = \frac{1 - \varphi_i}{1 + \left(\frac{\alpha}{2}\right)\varphi_i} \quad (21)$$

$$\frac{P_c}{P_o} = \frac{1 - \varphi_i}{1 + \frac{1}{3}\left(\frac{\alpha}{2}\right)\varphi_i} \quad (22)$$

where P_c , P_o , and α refer to the permeabilities of nanocomposite, polymer matrix, and nanofiber aspect ratio ($\alpha = 40$ for HNTs), respectively. In addition, φ_i can be calculated based on the following equation:

$$\frac{1}{\varphi_i} = 1 + \frac{\rho_i(1 - \mu_i)}{\rho_p\mu_i} \quad (23)$$

where ρ_i and μ_i are the density of impermeable phase ($\rho_i = 2.53$ g cm⁻³ for HNTs) and the weight fraction of impermeable phase, respectively. ρ_p is the density of the permeable phase, obtained by the following equation:

$$\rho_p = \sum_{x=1}^n \rho_x V_x \quad (24)$$

where ρ_x and V_x are the density and volume fraction of each component in the polymer blend ($\rho_{PS} = 1.04$ g cm⁻³ and $\rho_{POE} = 0.865$ g cm⁻³), respectively.

In addition, the Cussler model for regular and random nanofiller dispersions can be predicted according to Equations (25) and (26), respectively^[40]:

$$\frac{P_c}{P_o} = \frac{1 - \varphi_i}{1 + \left(\frac{\alpha}{2}\varphi_i\right)^2} \quad (25)$$

$$\frac{P_c}{P_o} = \frac{1 - \varphi_i}{\left(1 + \frac{\alpha}{3}\varphi_i\right)^2} \quad (26)$$

3. Experimental Section

3.1. Materials

General purpose PS (GPPS 1540 grade) with a melt flow index (MFI) of 11 g/10 min was purchased from Tabriz Petrochemical Company, Iran. POE (ethylene-1-octene copolymer, LC565 grade) with an MFI of 3.9 g/10 min and 38 wt% octene content was purchased from LG Chemical Company, South Korea. HNTs and PP-g-MAH ($M_n \approx 3900$ and $M_w \approx 9100$) were acquired from Sigma-Aldrich Company, Germany. The typical specific surface area and aspect ratio of HNTs were 64 m² g⁻¹ and 2.53 g cm⁻³, respectively. In addition, the diameter and length of HNTs were 30–70 nm and 1–3 μ m, respectively.

3.2. Specimen Preparation

The specimen preparation procedure is illustrated in **Figure 1**. The materials were initially dehumidified and dried in an oven at 80 °C for 4 h. They were then mixed for 8 min in a laboratory batch internal mixer (Brabender W350 EHT) with a rotor speed of 60 rpm and a temperature of 200 °C. Next, the specimens were compression-molded for 7 min at a pressure of 10 MPa to produce sheets with dimensions of 100 × 150 × 2 mm³. The specimen compositions are provided in **Table 1**.

3.3. Characterization and Testing

A scanning electron microscope (TESCAN VEGA SEM, Tescan Orsay Holding, Czech Republic) was used to investigate the morphology of the specimens. The dispersion of HNTs was studied using an energy-dispersive X-ray spectroscopy (EDS) instrument (Oxford INCA EDS (Oxford Instruments, UK). A transmission electron microscope operating at 100 kV (Philips EM208 TEM, Philips Corporation, Netherlands) was used to study the dispersion state of the HNTs within polymer blends. The tensile properties of the specimens were measured using a Geotech static hydraulic universal testing system according to ASTM D-638. The testing speed was 1 mm min⁻¹, and a load cell of 1 kN was used at room temperature. The tests were repeated three times, and the average results were reported.

The permeabilities of dry N₂ and CO₂ gases in the specimens were determined using a gas permeability tester (GDP-C, Brugger München GmbH, Germany). The test was performed at room temperature and under a pressure of 3 bar. The measured values were based on the Barrer (1 Barrer = 3.348 × 10⁻¹⁶ mol m (m² s Pa)⁻¹). During the test, a remote computer evaluated and displayed the pressure rise throughout the test time to calculate the permeability using the below equation:^[24,41]

$$P = \frac{273.15 \times 10^{10} V l}{760 AT \left(\frac{76P_0}{14.7}\right)} \left(\frac{dP}{dt}\right) \quad (27)$$

where P , V , T , A , l and P_0 are permeation coefficient (Barrer), volume of the downstream (cm³), temperature (K), area of the membrane (cm²), membrane thickness (μ m), and feed pressure (psi), respectively.

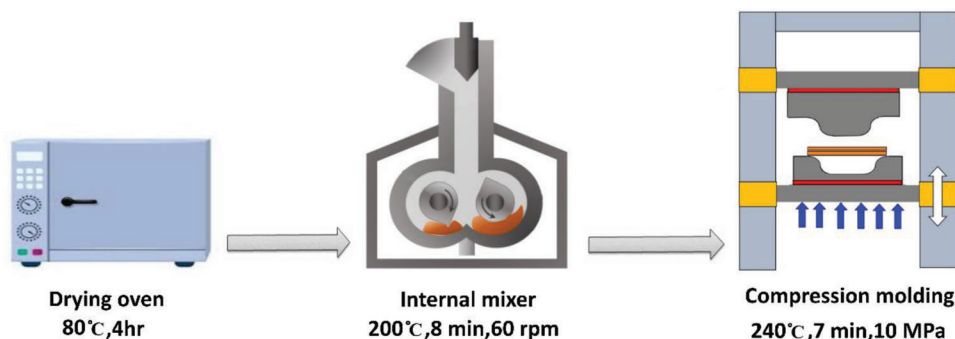


Figure 1. Specimen preparation procedure.

Table 1. Specimen compositions.

Specimen code	PS [wt%]	POE [wt%]	HNT [phr ^{a)}]	PP-g-MA [phr]
PS/POE 90/10	90	10	0	0
PS/POE/HNT 90/10/1	90	10	1	0
PS/POE/HNT 90/10/3	90	10	3	0
PS/POE/HNT 90/10/5	90	10	5	0
PS/POE/HNT/PP-g-MA 90/10/5/5	90	10	5	5
PS/POE 80/20	80	20	0	0
PS/POE/HNT 80/20/1	80	20	1	0
PS/POE/HNT 80/20/3	80	20	3	0
PS/POE/HNT 80/20/5	80	20	5	0
PS/POE/HNT/PP-g-MA 80/20/5/5	80	20	5	5

^{a)} Parts per hundred resin.

The samples' water vapor transmission (WVT) was calculated at 38 C using the methodology explained in the literature^[42] according to ASTM E96/E 96M-05. Films with a thickness of 0.1 mm were sealed by a rubber O-ring on top of Plexiglas test bottles containing dried silica gel. Afterward, films were placed in a glass desiccator with 200 mL saturated magnesium nitrate solution (50% relative humidity). Finally, test bottles were weighed periodically for 24 h, and the WVT was determined as follows:^[42]

$$WVT = (\Delta W/t)/A \quad (28)$$

Where ΔW denotes the weight gain of the tested bottles, t corresponds to the time during which ΔW happened, $\Delta W/t$ denotes the slope of the straight line in the diagram $\Delta W = f(t)$, and A is the permeation area.

3.4. Molecular Dynamics Simulation

The nanocomposite system consisted of model HNTs and a PS/POE blend, in which each polymer was composed of 20 repeating units. The gases considered were N_2 and CO_2 . All simulations were performed in BIOVIA Materials Studio (v7.0), where the initial structures of the model HNT and polymer blends were geometry-optimized using the smart algorithm and 1000 iterations. For all simulations performed in this work, the COMPASS

force field^[43] was used. The system components (HNTs, PS, POE, N_2 , and CO_2) were packed in different simulation cells using the Amorphous Cell module of Materials Studio, based on four different compositions (Specimens 1–4 in Table 2). The target density for the different systems was 0.95 g cm^{-3} , which yielded final simulation cell dimensions ranging from $25.2 \times 25.2 \times 25.2 \text{ \AA}^3$ for the PS/POE 90/10 blend systems to $28.3 \times 28.3 \times 28.3 \text{ \AA}^3$ for the PS/POE 80/20 blend systems.

Once the systems were created, thermal equilibration was performed at 300 K using the NPT ensemble for 50 ps (time step = 1 fs), followed by ramping the temperature to 500 K with the rate of 0.2 K ps^{-1} , annealing at this temperature for 250 ps and cooling the system temperature down to 300 K with the cooling rate of 0.2 K ps^{-1} . The average equilibrated densities of the systems were in the range of 0.93 to 0.97 g cm^{-3} . Next, production runs were carried out at 300 K using the NVT simulations (time step = 1 fs) for a total simulation time of 1 ns. Moreover, velocity rescaling was used to control the temperature. Trajectory data were output every 200 frames and used to calculate the diffusion coefficients of CO_2 and N_2 in PS/POE/HNT nanocomposite systems using Einstein's relation, which is based on mean-square displacement (MSD) data:^[44]

$$D = \frac{1}{6N} \lim_{t \rightarrow \infty} \frac{d}{dt} \left\{ \sum_i^N [r_i(t) - r_i(0)]^2 \right\} \quad (28)$$

Table 2. The compositions of the PS/POE and PS/POE/HNT systems.

Component (quantity)	PS/POE 90/10 blend system compositions				PS/POE 80/20 blend system compositions			
	System 1	System 2	System 3	System 4	System 1	System 2	System 3	System 4
PS (no. of chains)	4	4	4	4	5	5	5	5
POE (no. of chains)	1	1	1	1	3	3	3	3
HNT (mol per phr ^{a)})	0	2/1	4/3	6/5	0	2/1	4/3	6/5
N ₂ (no. of molecules)	2	2	2	2	2	2	2	2
CO ₂ (no. of molecules)	2	2	2	2	2	2	2	2

^{a)} Parts per hundred resin.

where N , $r_i(0)$, and $r_i(t)$ are the total number of diffusing atoms, position of diffusing atom i at time zero, and position of diffusing atom i at time t , respectively.

4. Results and Discussion

4.1. Morphological Studies

4.1.1. SEM–EDS Analyses

SEM imaging and EDS elemental mapping of Si in HNTs are used to compare the phase morphologies of the PS/POE/HNT nanocomposites, as shown in **Figure 2**. Overall, the SEM micrographs reveal a matrix (PS)-droplet (POE) morphology. Increasing the POE content from 10 to 20 wt% at a constant HNT content (1 or 5 phr) results in an increase in the average POE droplet size (compare between **Figure 2a,c** or **Figure 2b,d**). This observation may also be attributed to the “barrier” action of HNTs on the coalescence of the POE domains during melt blending. At low HNT content (1 phr), a good dispersion of the nanofillers in the PS/POE matrix is observed, which contributes to the formation of smaller POE droplets (elemental maps in **Figure 2a,c**). Similar observations have been reported by Kiani et al.^[14] for nanoclays in PS/POE blends, Haghnegahdar et al.^[45] for PP/ethylene propylene diene monomer/graphene nanocomposites, Kubade et al.^[46] for surface-modified HNTs in PP/ABS blends, and Lin et al.^[47] for HNTs in PP/poly(ethylene terephthalate) blends. On the contrary, at high HNT contents (5 phr), the increase in the POE domain sizes may be partially attributed to the HNT aggregation (elemental maps in **Figure 2b,d**) due to strong hydrogen bonding interactions that exist between the HNTs.^[48] As mentioned in our previous work,^[7] adding PP-g-MA to the PS/POE/HNT blend aids in the dispersion of HNTs in the PS/POE matrix and improves the interfacial adhesion between the POE and PS domains. This improvement can be ascribed to the interactions between the hydroxyl groups on the HNT surfaces with the maleic anhydride groups of PP-g-MA.

4.1.2. TEM Analyses

A TEM micrograph of HNTs is shown in **Figure 3**, illustrating the tubular structure of HNTs with variable sizes. The TEM micrographs of PS/POE/HNT nanocomposites with PS/POE ratios of 90/10 and 80/20 are provided in **Figures 4** and **5**, respectively.

As PS and POE are immiscible, the POE domains appear as discontinuous phases (bright areas) with uneven shapes scattered throughout the PS matrix (grey background) (**Figures 4** and **5**). In addition, the black domains in the TEM micrographs represent agglomerated HNTs, which are observed to be mainly located in the PS matrix and near the PS-POE interfaces, confirming the fact that HNTs have a compatibilizing effect. However, some localization of the HNTs is also observed within the POE domains at high HNT contents (5 phr) (**Figures 4c** and **5c**), which is again attributed to the HNT aggregation. With the addition of the PP-g-MA compatibilizer to the PS/POE blend with a high HNT content, nanofiller aggregation is somewhat reduced, notably at the PS-POE interfaces (**Figures 4d** and **5d**).

4.2. Mechanical Properties

The tensile strength (σ), tensile modulus (E), and elongation at break (ϵ) of the different PS/POE and PS/POE/HNT sheets are provided in **Table 3**. In addition, the effects of POE content on the tensile strength and modulus, as well as elongation at break, of the PS/POE sheets are plotted in **Figures 6** and **7**, respectively. The addition of POE to PS and increasing the POE content is observed to result in decreased tensile strength and tensile modulus of the neat PS sheet (**Table 3** and **Figure 6**). This observation is expected because POE has lower tensile strength and tensile modulus than those of PS.^[49–51] In addition, the immiscibility between PS and POE results in poor interfacial adhesion between the polymer domains, further contributing to the decrease in observed mechanical properties.^[16] Despite this mechanical property deterioration, an increase in the elongation at break of PS is observed with the addition of POE (**Figure 7**), that may be attributed to the improved ductility of the PS/POE sheet due to the presence of the elastomeric component. These results are consistent with the observations reported by Kiani et al.^[14] and Chen et al.^[52] Overall, the maximum reduction of tensile strength (16 MPa) and tensile modulus (677 MPa) occurred when 20 wt% POE was added to PS (**Figure 6**). On the other hand, the elongation at break of PS/POE 90/10 and PS/POE 80/20 sheets was 4.5% and 7.2%, respectively, which were both higher than that of PS (1.9%) (**Figure 7**).

The effects of HNT and PP-g-MA addition to the PS/POE blends on the mechanical properties of the resulting nanocomposite sheets are illustrated in **Figures 8** and **9**. The addition of 1 phr HNTs to the PS/POE matrix is observed to improve the tensile strength of the neat PS/POE 90/10 and PS/POE

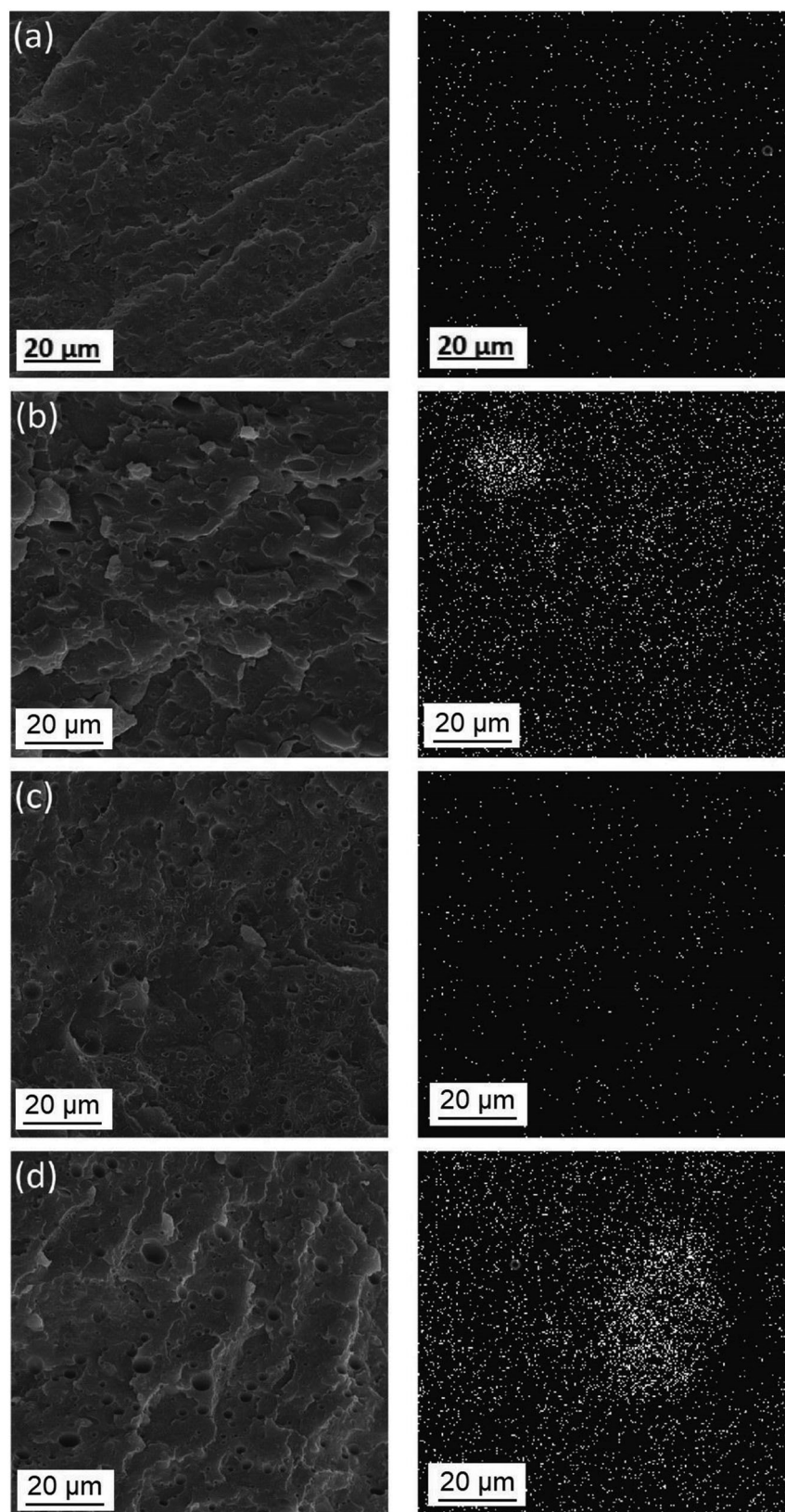


Figure 2. SEM micrographs (left) and EDS elemental maps (Si in HNTs) (right) of a) PS/POE/HNT 90 wt%/10 wt%/1 phr, b) PS/POE/HNT 90/10/5, c) PS/POE/HNT 80/20/1, and d) PS/POE/HNT 80/20/5 nanocomposites.

Table 3. Mechanical properties of the PS/POE and PS/POE/HNT sheets.

Specimen code	Tensile strength [MPa]	Tensile modulus [MPa]	Elongation at break [%]
PS	33.6 ± 0.3	1739.12 ± 37.0	1.9 ± 0.12
90/10	20.2 ± 0.7	1210.4 ± 43.0	4.5 ± 0.2
80/20	18.0 ± 0.64	1062.43 ± 30.7	7.2 ± 0.15
90/10/1	21.8 ± 1.0	1302.59 ± 39.5	4.9 ± 0.22
90/10/3	23.7 ± 0.9	1428.35 ± 48.0	4.1 ± 0.3
90/10/5	22.3 ± 1.5	1471.7 ± 40.0	3.7 ± 0.1
90/10/5/5	24.2 ± 0.8	1547.92 ± 55.6	3.2 ± 0.18
80/20/1	20.1 ± 1.0	1133.63 ± 36.0	7.9 ± 0.2
80/20/3	22.8 ± 0.8	1272.26 ± 39.0	7.4 ± 0.28
80/20/5	21.7 ± 1.2	1324.05 ± 41.0	6.2 ± 0.13
80/20/5/5	23.5 ± 0.5	1391.83 ± 29.5	5.3 ± 0.24

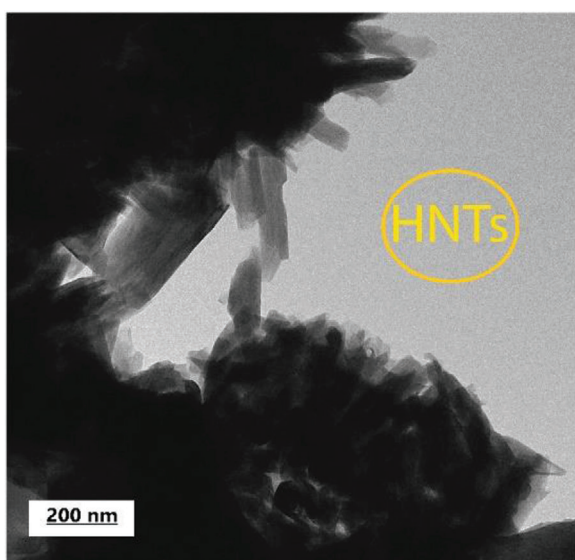


Figure 3. A TEM micrograph of HNTs.

80/20 sheets by 7.9% (Figure 8a) and 11.6% (Figure 9a), respectively. Moreover, increases in the tensile moduli of the neat PS/POE 90/10 and PS/POE 80/20 sheets by as much as 7.6% (Figure 8b) and 6.6% (Figure 9b) are observed, respectively. These improvements in the mechanical properties of the PS/POE/HNT nanocomposite sheets versus those of the PS/POE sheets are attributed to the sufficient stress transfer from the PS/POE matrix to the rigid HNTs because of the strong HNT-PS/POE interactions. It is worth noting that tensile strength in nanocomposites depends on the nanofiller content and level of stress transfer from the polymer matrix to the nanofiller, while tensile modulus depends on the rigidity of the nanocomposite components.^[53]

With an increase in the HNT content to 3 phr, the tensile strengths of both PS/POE 90/10 and PS/POE 80/20 nanocomposite sheets reach maxima (Figures 8a and 9a), whereafter reductions are observed in the average tensile strengths of the PS/POE sheets when the HNT content reaches 5 phr. However, these reductions are not statistically significant due to overlap-

ping error bars (Figures 8a and 9a). Nevertheless, these observations are again attributed to the HNT aggregation within the PS/POE matrix,^[54] which are also confirmed by observations in Figure 2b,d, as well as in Figures 4c and 5c. Contrary to tensile strengths, the tensile moduli of the PS/POE/HNT sheets continually increase with an increase in the HNT content up to values of 1472 MPa for the PS/POE 90/10 (Figure 8b) and 1324 MPa for the 80/20 nanocomposite sheets (Figure 9b), respectively. Based on these observations, the HNT dispersion in the PS/POE matrix seems not to affect the tensile modulus of the PS/POE/HNT nanocomposite sheet, which may be valid up to an HNT content of 5 phr used in this study. Similar observations have been previously reported for PS/poly(styrene-*b*-isoprene-*b*-styrene)/HNT nanocomposites^[55,56] and other HNT-containing polymer nanocomposites.^[22,57] By incorporating 5 phr PP-g-MA as a compatibilizer in the PS/POE/HNT nanocomposites with an HNT content of 5 phr, the average tensile strengths of both PS/POE 90/10 (Figure 8a) and PS/POE 80/20 sheets (Figure 9b) further increase; although, the improvements statistically remain at the same level as those for the other specimens (an HNT content of 3 phr and above). However, the tensile moduli of the PS/POE/HNT 90/10/5 (Figure 8b) and PS/POE/HNT 80/20/5 nanocomposite sheets are further increased by the addition of 5 phr PP-g-MA to the nanocomposites, possibly due to the HNT localization at the PS-POE interfaces. Overall, the above observations can be attributed to a combined effect of a decrease in the POE domain sizes (Figure 2), HNT localization in the PS-POE interfaces, and enhanced interfacial adhesion between the PS and POE domains when PP-g-MA is added to the PS/POE/HNT nanocomposites.^[7,58]

The elongations at break of the PS/POE 90/10 and PS/POE 80/20 sheets are 4.5% (Figure 8c) and 7.2% (Figure 9c), respectively. With the addition of 1 phr HNT to the PS/POE matrix, the elongations at break increase to 4.9% for the PS/POE 90/10 and 7.9% for the PS/POE 80/20 sheets, respectively, which are the highest among all specimens. Continuous decreases in the elongations at break of both PS/POE 90/10 and PS/POE 80/20 nanocomposite sheets are observed with further increase in the HNT content to 5 phr, as well as the addition of PP-g-MA. The enhancement in the elongations at break of the PS/POE/HNT sheets at low HNT contents (1 phr) over those of the PS/POE sheets may be attributed to the lubricating effect of

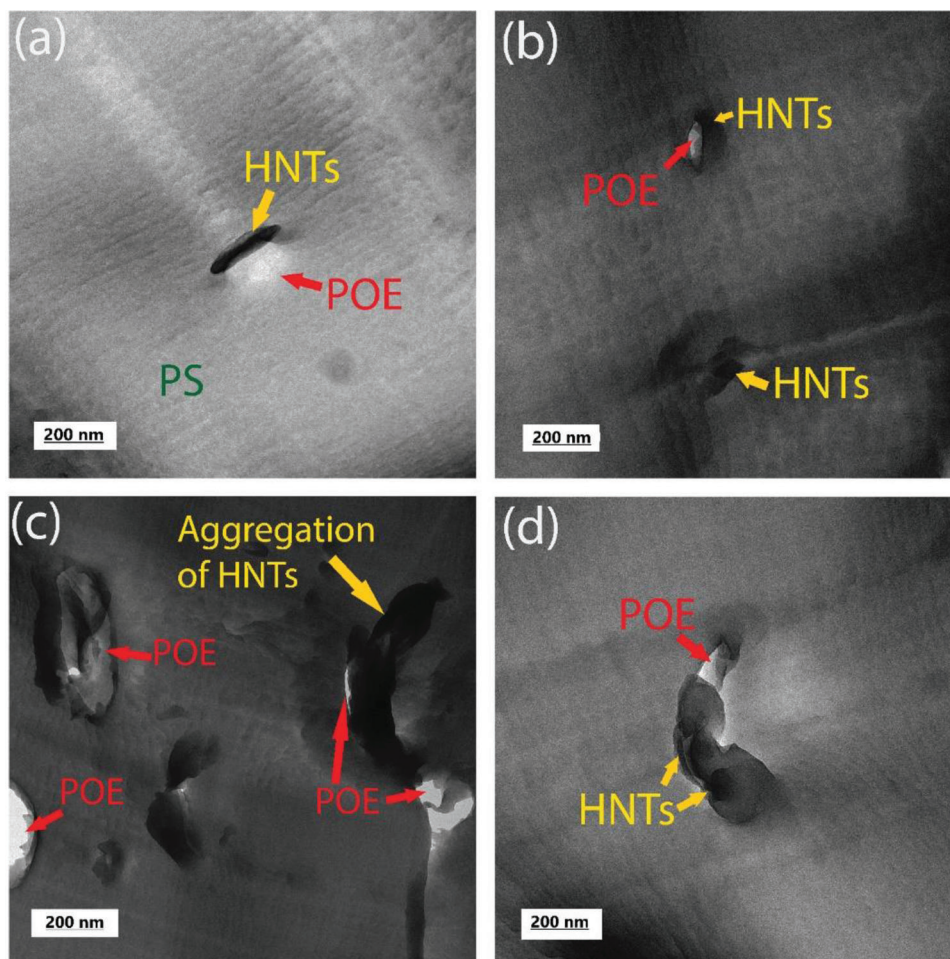


Figure 4. TEM micrographs of a) PS/POE/HNT 90 wt%/10 wt%/1 phr, b) PS/POE/HNT 90/10/3, c) PS/POE/HNT 90/10/5, and d) PS/POE/HNT/PP-g-MA 90/10/5/5 phr nanocomposites.

the HNTs at these loading levels, which has also been reported for PLA/EVA blends.^[48,59] At higher HNT contents, nanotubes can significantly restrict polymer matrix deformation, a situation that gets aggravated with the addition of PP-g-MA due its nanotube dispersing effect.^[60,61]

4.2.1. Theoretical Predictions of Mechanical Properties

The moduli of the PS/POE sheets were calculated for the different POE contents using the parallel (Voigt) (Equation (1)), series (Reuss) (Equation (2)), Hirsch (Equation (3)), Coran and Patel (Equations (4) and (5)), Barentsen 1 (parallel model of serial linked parts) (Equations (6) and (7)), and Barentsen 2 (series model of parallel parts) (Equations (8) and (9)) models, and the results are shown in **Figure 10**. The parallel and series models offer approximate predictions to identify the upper and lower bounds of the theoretical moduli, respectively. The upper-boundary model is better than the lower-boundary one in terms of the tensile modulus prediction (Figure 10). This implies that the iso-strain condition is more prominent than the iso-stress condition in the PS/POE blends. The Hirsch model

provides specific information about the validity of the parallel and series models through their combination. If the modulus determined by the Hirsch model equals the experimental data for all blends, the term x in Equation (3) can be obtained for each blend. A comparison of the x values indicates that, as the content of POE increases, the iso-stress assumption becomes more prevalent. The Coran and Patel model with $n = 64$ provides tensile modulus predictions closer to the experimental data. While the Barentsen 1 model provides tensile modulus predictions closer to the upper boundary values, the Barentsen 2 model give perfect tensile modulus predictions, matching the experimental values. The latter model is; hence, the most suitable one for the prediction of the tensile moduli of the PS/POE sheets.

The tensile moduli of the PS/POE/HNT nanocomposites were calculated using the Guth (Equation (10)), Halpin-Tsai (Equation (11)), Hui-Shia (Equations (12)–(14)), Paul (Equation (15)), Maxwell (Equation (16)), and Nielsen (Equations (17) and (18)) models, and the results are compared with the upper-boundary and lower-boundary model predictions in **Figure 11**. The tensile moduli predicted by the series, parallel, Maxwell, and Halpin-Tsai models all fail to match the experimental values. This

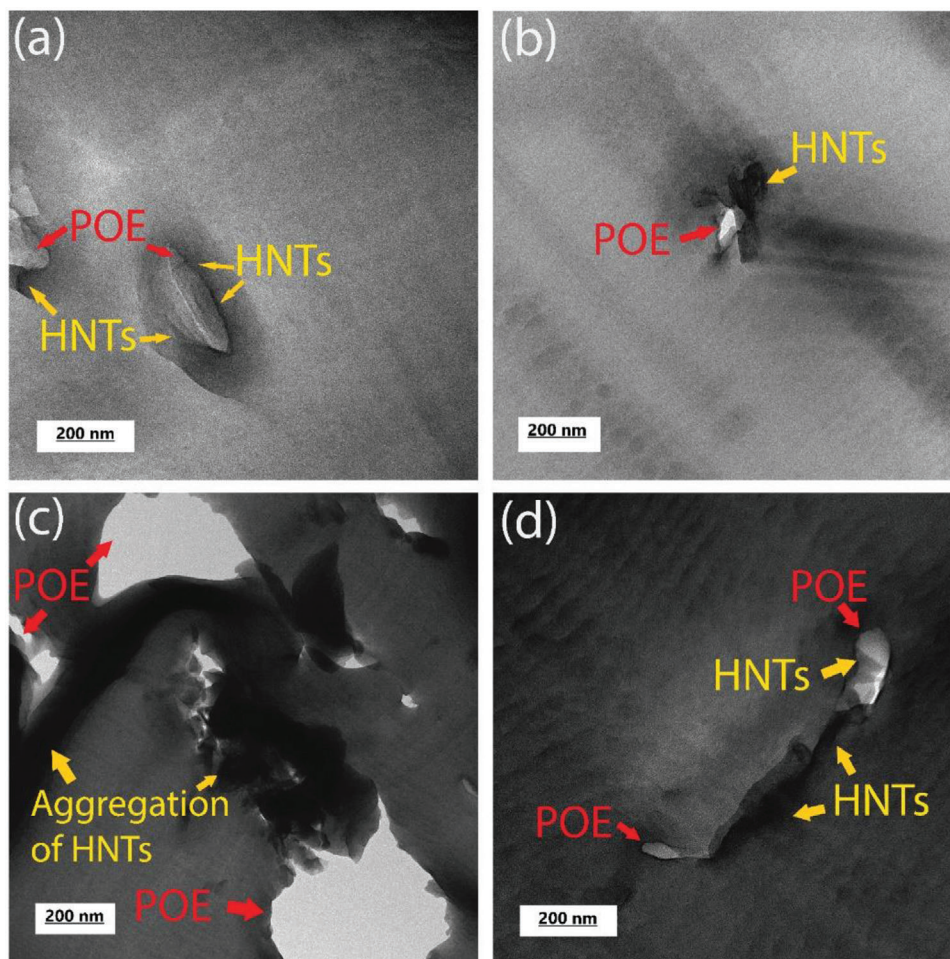


Figure 5. TEM micrographs of a) PS/POE/HNT 80 wt%/20 wt%/1 phr, b) PS/POE/HNT 80/20/3, c) PS/POE/HNT 80/20/5, and d) PS/POE/HNT/PP-g-MA 80/20/5/5 phr nanocomposites.

behavior is also observed for the Guth model predictions at higher HNT contents in the blends, which can be attributed to the non-linear term $(\alpha\varphi_f)^2$ in the model.^[28] Among the above-mentioned models, the Nielsen, Paul, and Hui-Shia models provide tensile modulus predictions that are closer to the experimental values.

Finally, the tensile strengths of the nanocomposites were calculated using the Pukanszky (Equation (19)) and Nikolais and Narkis (Equations (20) and (21)) models, and the results are shown in Figure 12. By fitting the Pukanszky model with the experimental values and assuming that σ_{ym} equals the tensile strength of the PS/POE blends, the empirical β parameter (Equation (19)) was determined to be 6.3803 and 10.798 for the PS/POE/HNT 90/10/0-5 and PS/POE/HNT 80/20/0-5 nanocomposites, respectively. The value of the β parameter depends on various factors, such as average nanofiller size, average polymer–nanofiller interfacial strength, and average polymer–nanofiller contact area. These factors affect the load-bearing capacity of the nanocomposites. As observed in Figure 12, the Pukanszky model provides more accurate estimations of the tensile strengths of the nanocomposites than the Nikolais and Narkis model.

4.3. Gas Permeabilities

Gas permeability is a significant property that needs to be analyzed for packaging films.^[62] Herein, the permeability coefficients for N_2 and CO_2 in the PS/POE sheets and PS/POE/HNT nanocomposite sheets were measured, and the results are shown in Figures 13 and 14, respectively. As the polarity of PS is lower than that of POE, the dissolution of the N_2 and CO_2 gases (both non-polar) in the PS domains is easier than in the POE domains. Therefore, the gas permeability coefficients for PS are larger than those of POE and as a consequence, a drop in gas permeability is observed with an increase in the POE content in the PS/POE blends (Figure 13).

The addition of up to 3 phr HNTs to the PS/POE blends leads to a decrease in the permeability of both N_2 and CO_2 gases (Figure 14). This observation is attributed to the good gas barrier property of the HNTs because of their hollow, tubular structure and high aspect ratio.^[25] However, increasing the HNT weight fraction to 5 phr results in a drop in the favorable gas barrier effect due to HNT aggregation.^[63] The nanocomposite morphology has a strong impact on its gas permeability. Overall, homogeneously distributed nanofillers in the polymer matrix provide a

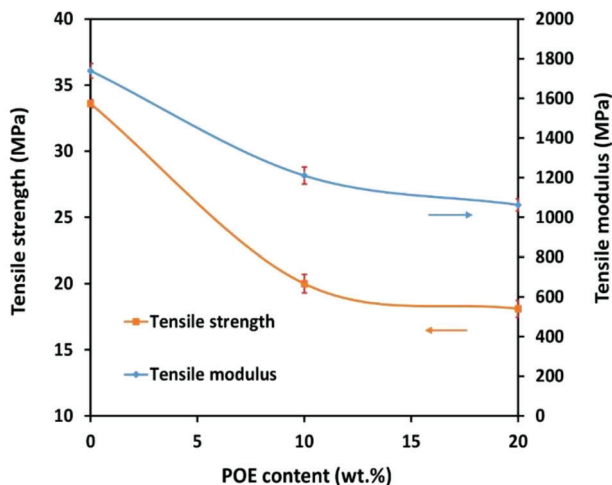


Figure 6. Tensile strengths and tensile moduli of the PS/POE sheets as functions of the POE content.

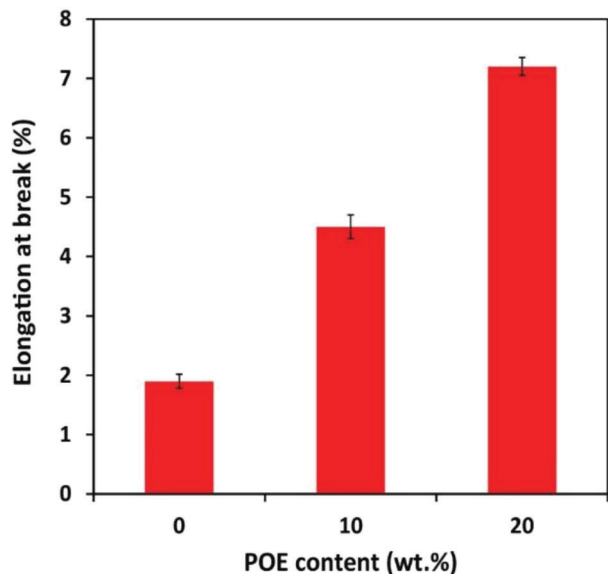


Figure 7. Elongation at break of the PS/POE sheets as a function of the POE content.

more tortuous path for the diffusing gas molecules; and thereby, improve the gas barrier property of the nanocomposite.^[24,64] The incorporation of PP-g-MA in the PS/POE/HNT blends with a high HNT content (5 phr) resulted again in reduced gas permeability (Figure 14), which is attributed to a better dispersion of the HNTs within the PS/POE matrix, as mentioned before.

4.3.1. Theoretical Predictions of Gas Permeabilities

The theoretical N_2 and CO_2 gas permeabilities, as predicted by the Nielsen and Cussler models (Equations (21)–(26)) for regular and random dispersions of the HNTs in the PS/POE/HNT nanocomposites are shown in **Figures 15** and **16**. As these mod-

els cannot predict the gas permeabilities of nanocomposites with nonuniform dispersions of nanofillers, only the PS/POE/HNT nanocomposites with demonstrated good HNT dispersions, that is, those containing 1 and 3 phr HNTs, as well as 5 phr HNTs and 5 phr PP-g-MA are selected for analysis. Overall, for a random dispersion of HNTs in the selected PS/POE/HNT nanocomposites, the N_2 and CO_2 gas permeabilities predicted by the Nielsen model are in much better agreement with the experimental data than those predicted by the Cussler model (Figures 15 and 16). However, the opposite is true, in general, with respect to the N_2 and CO_2 gas permeabilities in regular dispersions of the HNTs in the PS/POE/HNT nanocomposites. In other words, the Cussler model provides a better overall estimation of the gas permeabilities with some overprediction (Figures 15 and 16). The Nielsen–Random model seems to be more suitable for the PS/POE/HNT nanocomposites with lower HNT contents. Overall, the nanofiller content and dispersion in the polymer matrix, as well as other morphological features of the nanocomposites, should simultaneously be considered for a better prediction of gas permeabilities.

4.4. Gas Diffusion Coefficients

The calculated N_2 and CO_2 diffusion coefficients in the different PS/POE/HNT systems (Table 2) are provided in **Table 4**. Overall, incorporating HNTs in the PS/POE matrix results in a significant decrease in the diffusion of N_2 in the PS/POE/HNT 90/10/0-5 systems, an effect that gets more pronounced with an increase in the HNT content from 1 to 5 phr. However, no general trend is observed for the diffusion of CO_2 in the PS/POE/HNT 90/10/0-5 systems (Table 4). Unlike the case for the N_2 diffusion, incorporating HNTs in the PS/POE matrix causes an increase in the CO_2 diffusion coefficient at 1 phr HNT and a decrease back to the same diffusion coefficient value as that of the PS/POE 90/10 system with further increase in the HNT content. The N_2 and CO_2 diffusion coefficients in the PS/POE/HNT 80/20/0-5 systems are in general lower than the corresponding values for the PS/POE/HNT 90/10/1-5 systems, signifying the fact that a larger POE content in the PS/POE blend leads to a lower gas diffusion coefficient, as stated earlier (Table 4).

Except for the anomalous increase in the N_2 and CO_2 gas diffusion coefficients in the PS/POE/HNT 80/20/3 system, an overall decrease in the gas diffusion coefficients is observed with an increase in the HNT content in the PS/POE/HNT 80/20/0-5 systems (Table 4). As a final observation, the lowest N_2 and CO_2 diffusion coefficients are attained in the PS/POE/HNT 90/10/5 and PS/POE/HNT 80/20/5 system, respectively.

4.5. Water Vapor Transmission (WVT)

Table 5 indicates the WVT rate of films. As observed, the PS film had the highest rate compared to other films. Besides, incorporating POE lowered the WVT; the more POE contents, the less the WVT. This could be due to the greater intrinsic polarity of the phase POE compared to PS. Adding HNTs had the same effect as POE on the WVT, with the difference that it was more dominant. This result can be attributed to gas molecules in nanocomposites

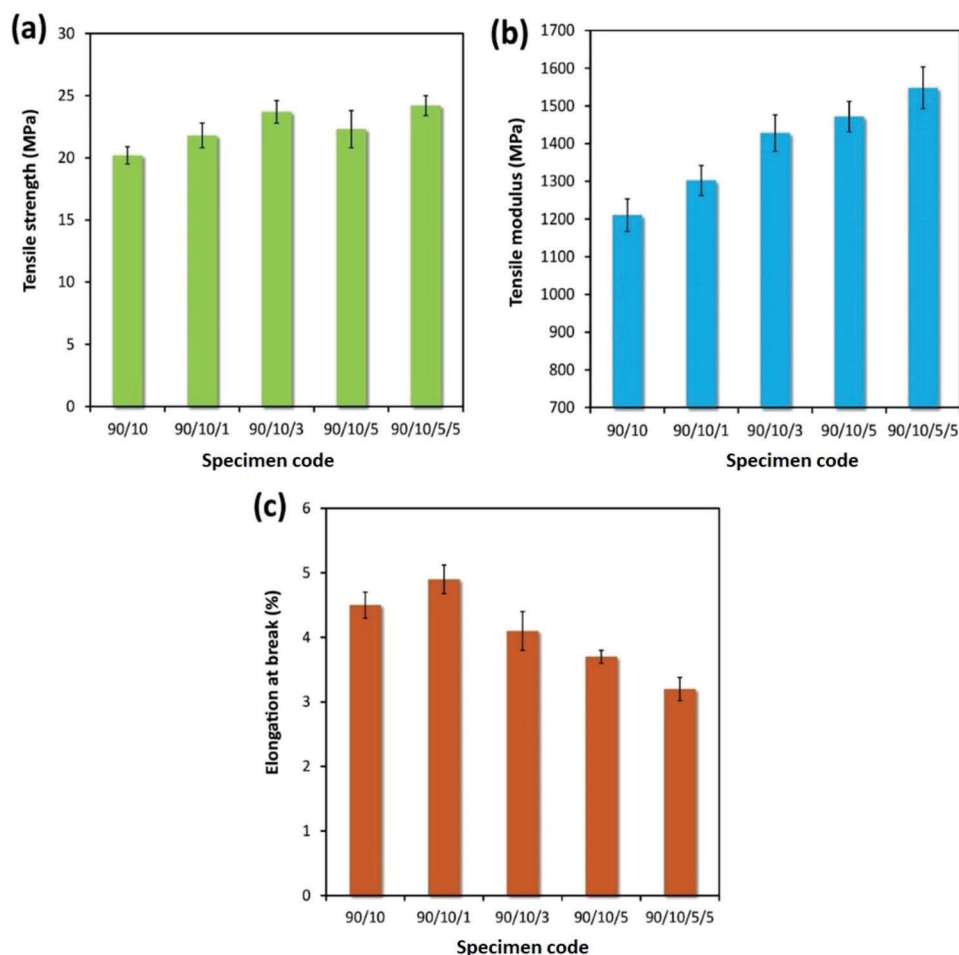


Figure 8. a) Tensile strength, b) tensile modulus, and c) elongation at break of the PS/POE 90 wt%/10 wt%, PS/POE/HNT 90/10/(1–5 phr), and PS/POE/HNT/PP-g-MA 90/10/5/5 phr sheets.

Table 4. Diffusion coefficients of N₂ and CO₂ in the different PS/POE/HNT systems.

System	Diffusion coefficient (Å ² ps ⁻¹)	
	N ₂	CO ₂
PS/POE 90/10	4.557×10^{-2}	1.343×10^{-4}
PS/POE/HNT 90/10/1	1.316×10^{-2}	4.393×10^{-4}
PS/POE/HNT 90/10/3	9.082×10^{-3}	3.163×10^{-4}
PS/POE/HNT 90/10/5	5.500×10^{-4}	1.343×10^{-4}
PS/POE 80/20	5.599×10^{-3}	8.333×10^{-5}
PS/POE/HNT 80/20/1	2.304×10^{-3}	2.628×10^{-5}
PS/POE/HNT 80/20/3	1.291×10^{-2}	2.413×10^{-4}
PS/POE/HNT 80/20/5	7.794×10^{-3}	4.931×10^{-6}

having to take a long and tortuous way around the impermeable HNTs distributed in the polymer matrix, compared with neat polymers in which gas penetration is much easier.^[40] However, when HNTs content was further increased, their barrier effect was sacrificed due to their accumulation. Moreover, adding compatibilizer led to decreased WVT, which can be attributed to the better dispersion of HNTs.

5. Conclusion

In this study, a series of polystyrene/polyolefin elastomer/Halloysite nanotube (PS/POE/HNT) nanocomposite sheets was fabricated with different polymer/nanofiller proportions using melt blending. The effects of HNTs on the mechanical and gas barrier properties of the nanocomposite

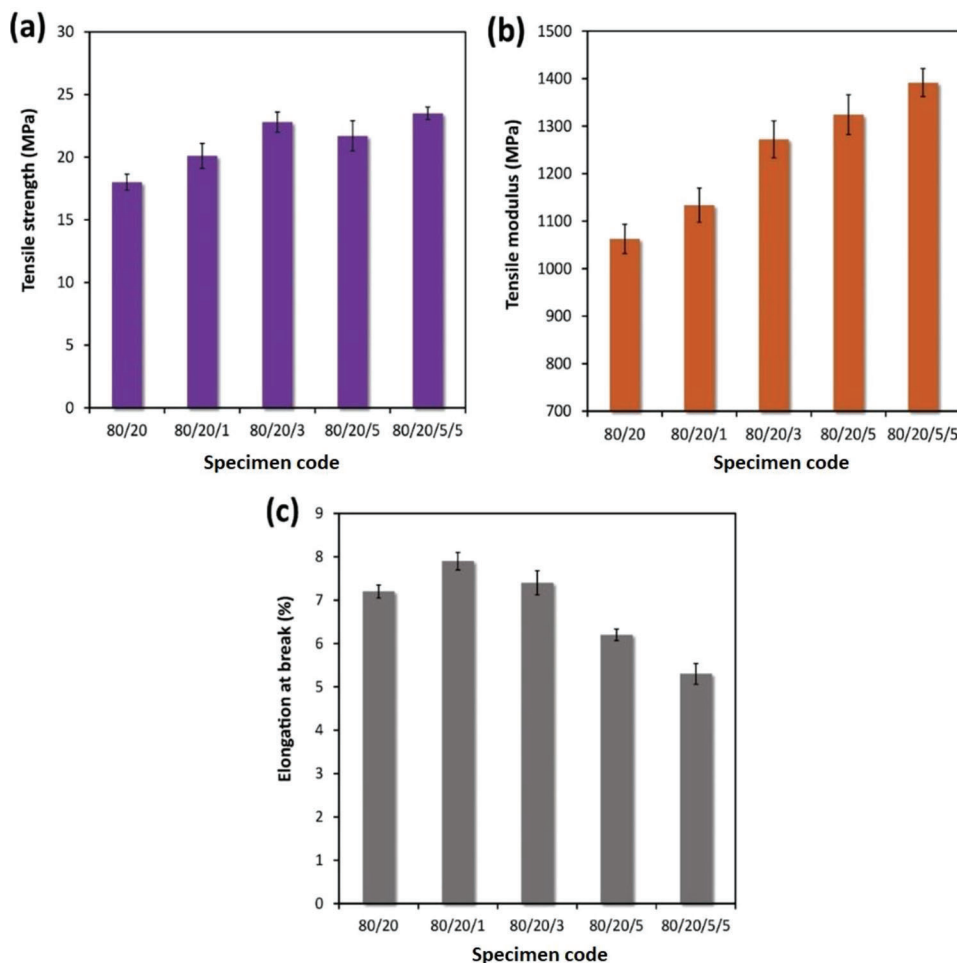


Figure 9. a) Tensile strength, b) tensile modulus, and c) elongation at break of the PS/POE 80 wt%/20 wt%, PS/POE/HNT 80/20/(1–5 phr), and PS/POE/HNT/PP-g-MA 80/20/5/5 phr sheets.

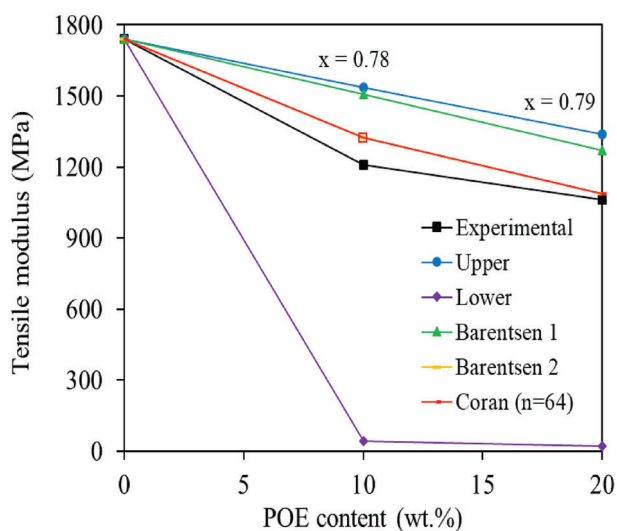


Figure 10. Comparison between the experimental and theoretical tensile moduli of the PS/POE sheets with various POE contents.

Table 5. Water vapor transmission values for materials.

Sample code	WVT [g h m^{-2}]
PS	2.53
90/10	2.39
80/20	2.25
90/10/1	2.19
90/10/3	1.80
90/10/5	1.93
90/10/5/5	1.65
80/20/1	2.00
80/20/3	1.70
80/20/5	1.79
80/20/5/5	1.57

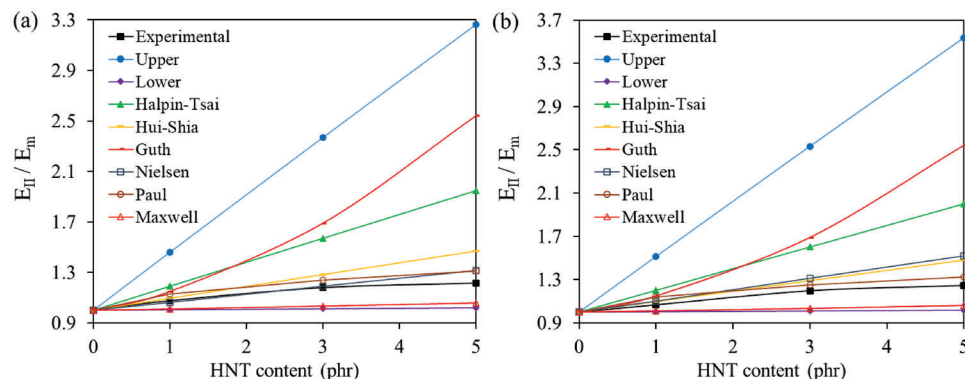


Figure 11. Comparison between the experimental and theoretical tensile moduli of a) PS/POE/HNT 90/10/0-5 and b) PS/POE/HNT 80/20/0-5 nanocomposites.

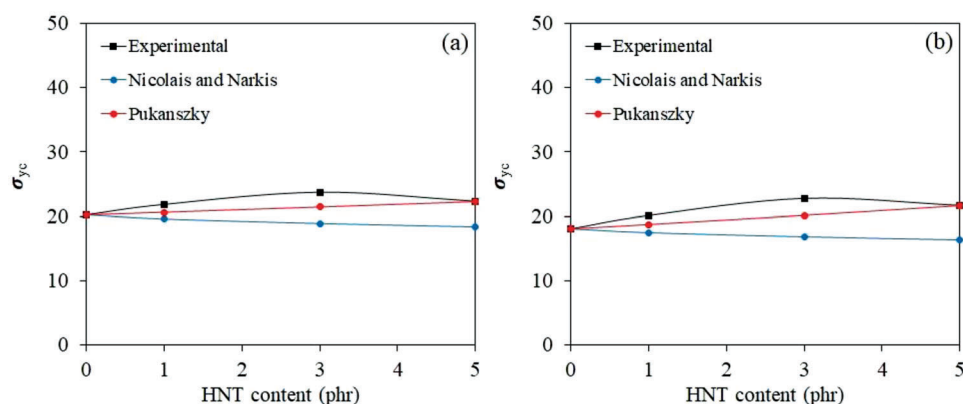


Figure 12. Comparison between the experimental data and theoretical tensile strengths of a) PS/POE/HNT 90/10/0-5 and b) PS/POE/HNT 80/20/0-5 nanocomposites.

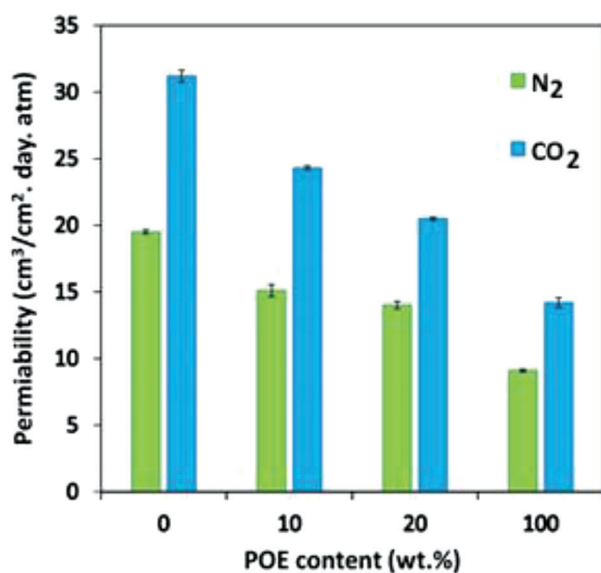


Figure 13. Gas permeabilities of the PS/POE blends.

sheets were further investigated using both experiments and theoretical calculations. Overall, blending PS with POE led to an increase in the elongation at break of PS, while its tensile

strength and tensile modulus decreased. Addition of HNTs to the PS/POE matrix (up to five parts per hundred resin (phr)) led to a linear increase in tensile modulus, while tensile strength reached a maximum at 3 phr HNTs with some strength deterioration at higher HNT contents due to nanofiller aggregation. The incorporation of maleic anhydride grafted polypropylene (PP-g-MA) in the PS/POE/HNT nanocomposites containing 5 phr HNTs resulted in better nanofiller dispersion in the PS/POE matrix; and hence, improved mechanical properties. The same PS/POE/HNT/PP-g-MA nanocomposite system exhibited lower N_2 and CO_2 gas permeabilities than those observed for the nanocomposite system without the PP-g-MA compatibilizer. In addition, incorporating POE and HNTs lowered PS's water vapor transmission (WVT), and the effect of HNTs was more dominant. Moreover, adding compatibilizer led to a further decrement in WVT, attributed to the better dispersion of HNTs. From a theoretical perspective, the best models for the prediction of tensile and gas barrier properties of the nanocomposites were determined. Finally, the N_2 and CO_2 diffusion coefficients were obtained using molecular dynamics simulations and the calculated values were used to explain the experimental observations. Based on the findings of this work, the PS/POE/HNT/PP-g-MA nanocomposites can be considered as suitable materials for packaging film applications.

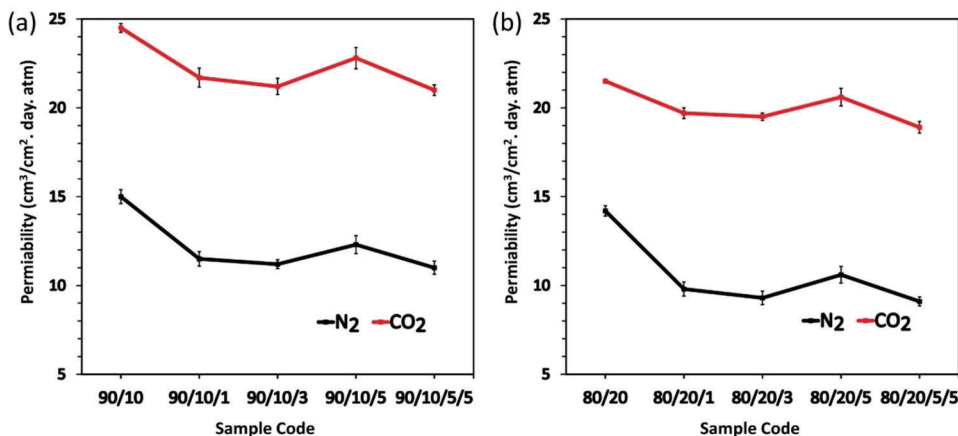


Figure 14. Gas permeabilities of a) PS/POE/HNT 90/10/0-5 and PS/POE/HNT/PP-g-MA 90/10/5/5, as well as b) PS/POE/HNT 80/20/0-5 and PS/POE/HNT/PP-g-MA 80/20/5/5 nanocomposites.

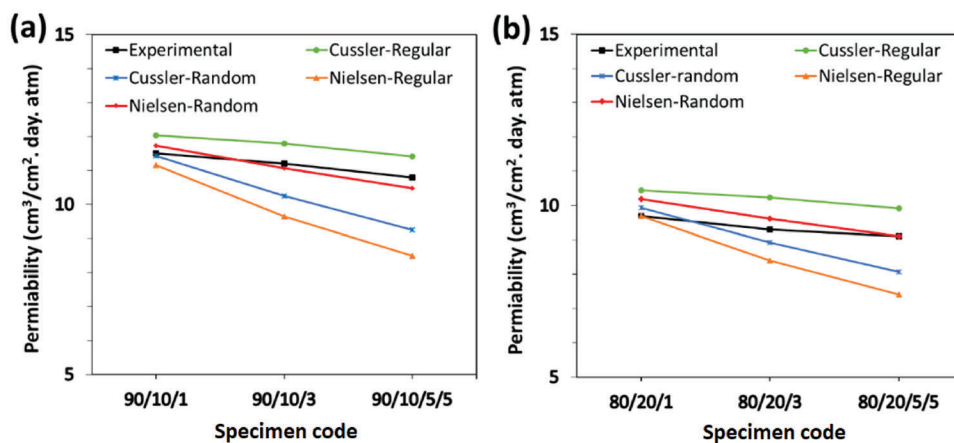


Figure 15. Theoretical predictions of N₂ permeabilities of a) PS/POE/HNT 90/10/1-3 and PS/POE/HNT/PP-g-MA 90/10/5/5, as well as b) PS/POE/HNT 80/20/1-3 and PS/POE/HNT/PP-g-MA 80/20/5/5 nanocomposites.

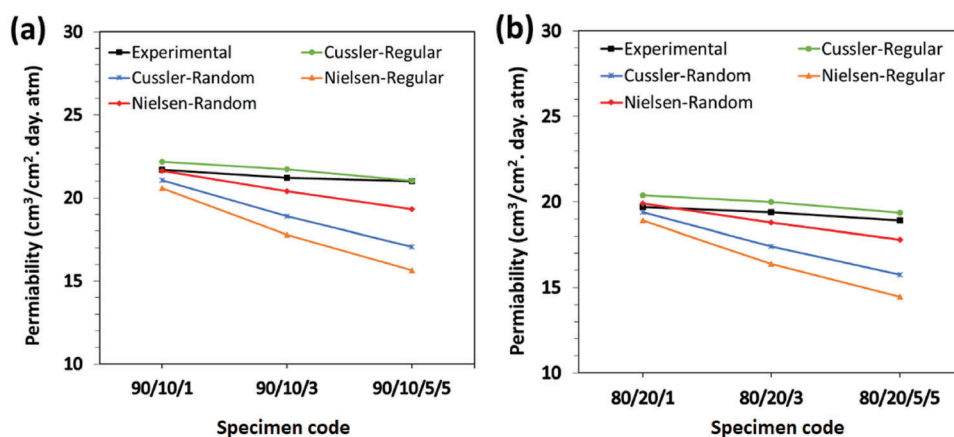


Figure 16. Theoretical predictions of CO₂ permeabilities of a) PS/POE/HNT 90/10/1-3 and PS/POE/HNT/PP-g-MA 90/10/5/5, as well as b) PS/POE/HNT 80/20/1-3 and PS/POE/HNT/PP-g-MA 80/20/5/5 nanocomposites.

Acknowledgements

This project was funded in part by the Iran Polymer and Petrochemical Institute (IPPI) and Bayreuth University within the framework of the Excellence Strategy of the German Federation and the States.

Open Access funding enabled and organized by projekt DEAL.

Conflict of Interest

The authors declare no conflict of interest.

Data Availability Statement

The data that support the findings of this study are available from the corresponding author upon reasonable request.

Keywords

gas permeability, halloysite nanotubes, mechanical properties, polyolefin elastomers, polystyrene

Received: March 9, 2023

Revised: May 4, 2023

Published online: May 18, 2023

- [1] B. Tajeddin, M. Arabkhedri, in *Polymer Science and Innovative Applications: Materials, Techniques, and Future Developments* (Eds: M. A. A. AlMadeed, D. Ponnamma, M. A. Carignano), Elsevier, Amsterdam, the Netherlands **2020**, p. 525.
- [2] R. Mokhtari Aghdami, S. R. Mousavi, S. Estaji, R. K. Dermeni, H. A. Khonakdar, A. Shakeri, *Polym. Compos.* **2022**, 43, 4165.
- [3] A. Paydayesh, S. R. Mousavi, S. Estaji, H. A. Khonakdar, M. A. Nozarinya, *Polym. Compos.* **2022**, 43, 411.
- [4] S. Gilakhakimabadi, M. Ehsani, H. A. Khonakdar, M. Ghaffari, S. H. Jafari, *Food Packag. Shelf Life* **2019**, 22, 100392.
- [5] A. F. Ghanem, A. M. Youssef, M. H. Abdel Rehim, *J. Mater. Sci.* **2020**, 55, 4685.
- [6] S. Dixit, V. L. Yadav, *Polym. Bull.* **2020**, 77, 1307.
- [7] M. I. Tayouri, S. R. Mousavi, S. Estaji, S. Nemat Mahand, R. Jahanmardi, M. Arjmand, K. Arnhold, H. A. Khonakdar, *Polym. Adv. Technol.* **2022**, 33, 2149.
- [8] A. Arora, V. Choudhary, D. K. Sharma, *J. Polym. Res.* **2011**, 18, 843.
- [9] B. Akbari, R. Bagheri, *Mech. Mater.* **2016**, 103, 11.
- [10] M. Goodarzi, G. Pircheraghi, H. A. Khonakdar, V. Altstadt, *Polym. Adv. Technol.* **2022**, 33, 937.
- [11] M. Entezam, H. Poormadadkar, H. A. Khonakdar, S. H. Jafari, *J. Appl. Polym. Sci.* **2020**, 137, 48791.
- [12] B. Zhu, W. Li, J. Song, J. Wang, *J. Macromol. Sci., Part B: Phys.* **2019**, 58, 73.
- [13] N. R. Savadekar, K. Jadhav, M. Mali, S. T. Mhaske, *Int. J. Plast. Technol.* **2014**, 18, 157.
- [14] F. Kiani, M. Entezam, H. A. Khonakdar, S. H. Jafari, C. Callsen, V. Altstadt, *J. Appl. Polym. Sci.* **2020**, 137, 48748.
- [15] S. N. Mahand, A. Yazdanbakhsh, M. I. Tayouri, A. Zarei, S. Nouranian, H. Ruckdäschel, H. A. Khonakdar, *Polym. Test.* **2023**, 120, 107960.
- [16] M. Entezam, H. A. Khonakdar, A. A. Yousefi, S. H. Jafari, U. Wagenknecht, G. Heinrich, *Mater. Des.* **2013**, 45, 110.
- [17] B. Baghaei, S. H. Jafari, H. A. Khonakdar, I. Rezaeian, L. As'habi, S. Ahmadian, *Polym. Bull.* **2009**, 62, 255.
- [18] V. Sangeetha, D. Gopinath, R. Prithivirajan, V. Girish Chandran, R. Manoj Kumar, *Polym. Test.* **2020**, 89, 106595.
- [19] P. Rajae, F. Ashenai Ghasemi, M. Fasihi, A. Sadeghi, B. Kakeh, *Polym. Compos.* **2022**, 43, 4495.
- [20] N. Karimpour-Motlagh, H. A. Khonakdar, S. H. Jafari, M. Panahi-Sarmad, A. Javadi, S. Shojaei, V. Goodarzi, *Polym. Adv. Technol.* **2019**, 30, 2695.
- [21] D. H. Kim, Y. S. Ryu, S. H. Kim, *Polym. Adv. Technol.* **2018**, 29, 2655.
- [22] P. R. Kubade, P. Tambe, H. B. Kulkarni, *Adv. Compos. Lett.* **2017**, 26, 182.
- [23] S. H. Lee, M. Kontopoulou, C. B. Park, *Polymer* **2010**, 51, 1147.
- [24] H. Ebadi-Dehaghani, M. Barikani, H. A. Khonakdar, S. H. Jafari, U. Wagenknecht, G. Heinrich, *Polym. Test.* **2015**, 45, 139.
- [25] Z. W. Abdullah, Y. u Dong, N. Han, S. Liu, *Composites, Part B* **2019**, 174, 107033.
- [26] T. S. Chow, *J. Mater. Sci.* **1980**, 15, 1873.
- [27] S. Ahmed, F. R. Jones, *J. Mater. Sci.* **1990**, 25, 4933.
- [28] B. Ghassemi, S. Estaji, S. R. Mousavi, S. Nemat Mahand, S. Shojaei, M. Mostafaiyan, M. Arjmand, H. A. Khonakdar, *J. Mater. Sci.* **2022**, 57, 7250.
- [29] J. A. Gopi, G. B. Nando, *Adv. Polym. Sci. Technol.: Int. J.* **2014**, 4, 43.
- [30] H. Veenstra, P. C. J. Verkooijen, B. J. J. Van Lent, J. Van Dam, A. P. De Boer, A. P. H. J. Nijhof, *Polymer* **2000**, 41, 1817.
- [31] E. Guth, *Rubber Chem. Technol.* **1945**, 18, 596.
- [32] T. D. Fornes, D. R. Paul, *Polymer* **2003**, 44, 4993.
- [33] R. Hill, *J. Mech. Phys. Solids* **1964**, 12, 199.
- [34] N. Dayma, B. K. Satapathy, *Mater. Des.* **2010**, 31, 4693.
- [35] B. Paul, Prediction of elastic constants of multi-phase materials, **1959**.
- [36] Y. Ohama, *Mater. J.* **1987**, 84, 511.
- [37] Y. Rao, J. M. Pochan, *Macromolecules* **2007**, 40, 290.
- [38] M. Narkis, L. Nicolais, *J. Appl. Polym. Sci.* **1971**, 15, 469.
- [39] B. Tan, N. L. Thomas, *J. Membr. Sci.* **2016**, 514, 595.
- [40] Z. W. Abdullah, Y. u Dong, I. J. Davies, S. Barbhuiya, *Polym.-Plast. Technol. Eng.* **2017**, 56, 1307.
- [41] D. Battegazzore, S. Bocchini, A. Frache, *eXPRESS Polym. Lett.* **2011**, 5, 849.
- [42] A. Giannakas, C. G. Spanos, N. Kourkoumelis, T. Vaimakis, A. Ladavos, *Eur. Polym. J.* **2008**, 44, 3915.
- [43] H. Sun, P. Ren, J. R. Fried, *Comput. Theor. Polym. Sci.* **1998**, 8, 229.
- [44] M. Kotelyanskii, D. N. Theodorou, *Simulation Methods for Polymers*, CRC Press, Boca Raton, FL **2004**.
- [45] M. Haghnegahdar, G. Naderi, M. H. R. Ghoreishy, *Compos. Sci. Technol.* **2017**, 141, 83.
- [46] P. Kubade, P. Tambe, *Compos. Interfaces* **2017**, 24, 469.
- [47] T. Lin, L. Zhu, T. Chen, B. Guo, *J. Appl. Polym. Sci.* **2013**, 129, 47.
- [48] R. K. Singla, S. N. Maiti, A. K. Ghosh, *J. Mater. Sci.* **2016**, 51, 10278.
- [49] A. S. Dike, U. Yilmazer, *J. Thermoplast. Compos. Mater.* **2020**, 33, 554.
- [50] P. Rajae, F. Ashenai Ghasemi, M. Fasihi, M. Saberian, *Composites, Part B* **2019**, 173, 106803.
- [51] L. Yang, H. Chen, S. Jia, X. Lu, J. Huang, X. Yu, K. Ye, G. He, J. Qu, *J. Appl. Polym. Sci.* **2014**, 131, 40660.
- [52] X. Chen, J. Yu, Z. Luo, S. Guo, M. He, Z. Zhou, *Polym. Adv. Technol.* **2011**, 22, 657.
- [53] S. K. Esthappan, S. K. Kuttappan, R. Joseph, *Polym. Degrad. Stab.* **2012**, 97, 615.
- [54] S. Bagheri-Kazemabad, D. Fox, Y. Chen, L. M. Geever, A. Khavandi, R. Bagheri, C. L. Higginbotham, H. Zhang, B. Chen, *Compos. Sci. Technol.* **2012**, 72, 1697.
- [55] E. Tekay, *J. Thermoplast. Compos. Mater.* **2020**, 33, 1125.
- [56] M. Makaremi, P. Pasbakhsh, G. Cavallaro, G. Lazzara, Y. K. Aw, S. M. Lee, S. Milioto, *ACS Appl. Mater. Interfaces* **2017**, 9, 17476.
- [57] Y. Guo, S. He, K. Yang, Y. Xue, X. Zuo, Y. Yu, Y. Liu, C.-C. Chang, M. H. Rafailovich, *ACS Appl. Mater. Interfaces* **2016**, 8, 17565.
- [58] D.-H. Lee, Y.-W. Chang, K.-S. Jang, *Materials* **2020**, 14, 27.

- [59] A. Zubkiewicz, A. Szymczyk, S. Paszkiewicz, R. Jedrzejewski, E. Piesowicz, J. Sieminski, *J. Appl. Polym. Sci.* **2020**, *137*, 49135.
- [60] Z. Xu, S. Jerrams, H. Guo, Y. Zhou, L. Jiang, Y. Gao, L. Zhang, L. Liu, S. Wen, *Int. J. Fatigue* **2020**, *131*, 105388.
- [61] O. H. Lin, H. M.d Akil, Z. A. M. Ishak, *Adv. Compos. Lett.* **2009**, *18*, 77.
- [62] A. Salehi, S. H. Jafari, H. A. Khonakdar, H. Ebadi-Dehaghani, *J. Appl. Polym. Sci.* **2018**, *135*, 46665.
- [63] C. E. Tas, S. Hendessi, M. Baysal, S. Unal, F. C. Cebeci, Y. Z. Menciloglu, H. Unal, *Food Bioprocess Technol.* **2017**, *10*, 789.
- [64] V. Prattipati, Y. S. Hu, S. Bandi, D. A. Schiraldi, A. Hiltner, E. Baer, S. Mehta, *J. Appl. Polym. Sci.* **2005**, *97*, 1361.